AGU PUBLICATIONS

Geophysical Research Letters

RESEARCH LETTER
10.1002/2017GL076311

Key Points:
- Neoarchean nanoparticle silicate inclusions appear to be the earliest iron mineral preserved in cherts from Australia and South Africa
- Our multiscale analyses indicate that the particles are greenalite that are dominantly Fe(II) with have low and variable Fe(III) content
- We present four (bio)geochemical hypotheses that could produce low-Fe(III) greenalite

Supporting Information:
- Supporting Information S1

Correspondence to:
J. E. Johnson,
jenaje@umich.edu

Citation:
Johnson, J. E., Muhling, J. R., Cosmidis, J., Rasmussen, B., & Templeton, A. S. (2018). Low-Fe(III) Greenalite was a primary mineral from Neoarchean oceans. *Geophysical Research Letters*, *45*, 3182–3192. https://doi.org/10.1002/2017GL076311

Received 5 NOV 2017
Accepted 21 FEB 2018
Accepted article online 27 FEB 2018
Published online 2 APR 2018

Low-Fe(III) Greenalite Was a Primary Mineral From Neoarchean Oceans

Jena E. Johnson[1,2], Janet R. Muhling[3,4], Julie Cosmidis[1,5], Birger Rasmussen[4], and Alexis S. Templeton[1]

[1]Department of Geosciences, University of Colorado Boulder, Boulder, CO, USA, [2]Now at Department of Earth and Environmental Sciences, University of Michigan, Ann Arbor, MI, USA, [3]School of Earth Sciences, University of Western Australia, Crawley, Western Australia, Australia, [4]Department of Applied Geology, Curtin University, Perth, Western Australia, Australia, [5]Now at Department of Geosciences, Pennsylvania State University, University Park, PA, USA

Abstract Banded iron formations (BIFs) represent chemical precipitation from Earth's early oceans and therefore contain insights into ancient marine biogeochemistry. However, BIFs have undergone multiple episodes of alteration, making it difficult to assess the primary mineral assemblage. Nanoscale mineral inclusions from 2.5 billion year old BIFs and ferruginous cherts provide new evidence that iron silicates were primary minerals deposited from the Neoarchean ocean, contrasting sharply with current models for BIF inception. Here we used multiscale imaging and spectroscopic techniques to characterize the best preserved examples of these inclusions. Our integrated results demonstrate that these early minerals were low-Fe(III) greenalite. We present potential pathways in which low-Fe(III) greenalite could have formed through changes in saturation state and/or iron oxidation and reduction. Future constraints for ancient ocean chemistry and early life's activities should include low-Fe(III) greenalite as a primary mineral in the Neoarchean ocean.

Plain Language Summary Chemical precipitates from Earth's early oceans hold clues to ancient seawater chemistry and biological activities, but we first need to understand what the original minerals were in ancient marine deposits. We characterized nanoscale mineral inclusions from 2.5 billion year old banded iron formations and determined that the primary minerals were iron-rich silicate minerals dominated by reduced iron, challenging current hypotheses for banded iron formation centered on iron oxides. Our results suggest that our planet at this time had a very reducing ocean and further enable us to present several biogeochemical mineral formation hypotheses that can now be tested to better understand the activities of early life on ancient Earth.

1. Introduction

For the first half of Earth's ~4.5 billion year history, there was negligible atmospheric oxygen and the oceans had high levels of ferrous iron and silica. The sedimentary record from 3.8 to 2.3 billion years ago (Ga) documents the survival of oxygen-sensitive detrital grains in conglomerates and marine sandstones (Johnson et al., 2014; Rasmussen & Buick, 1999), the lack of terrestrial iron oxidation in paleosols (Prasad & Roscoe, 1996; Rye & Holland, 1998), and an unfamiliar sulfur cycle with strong signals of photochemical reactions occurring in the absence of an ozone layer (Farquhar et al., 2011). Another conspicuous difference from modern marine sediments was the deposition of extensive silica-rich banded iron formations (BIFs) in the early oceans. These laminated BIFs are thought to be composed of chemical precipitates accumulating in ferruginous and silica-rich oceans (Bekker et al., 2014; Beukes & Gutzmer, 2008). BIFs have been extensively investigated as one of the best records of marine chemistry in the Archean (4.0–2.5 Ga) oceans (e.g., Klein, 2005). However, it is also well established that these BIFs have experienced early and late diagenesis, fluid flow, and metamorphism over their multibillion-year existence, and therefore, many—if not all—minerals in BIFs are attributed to diagenesis and later alteration (e.g., Bekker et al., 2014; Beukes, 1984; Fischer & Knoll, 2009; Klein, 2005; Pufahl & Hiatt, 2012; Simonson, 2003). Identifying the original precipitate(s) of BIFs has therefore been a critical question pertinent to understanding what BIFs represent and record with respect to ancient seawater chemistry and early life. While it is impossible to pinpoint the amorphous precursor phases that originally formed in the water column, it is possible to determine the first stable crystalline minerals that formed under Archean ocean conditions and were preservable in the rock record—which we will call the "primary mineral(s)."

While initial suggestions of primary BIF minerals concentrated on iron silicates like glauconite or greenalite (Leith, 1903; Spurr, 1894; Winchell et al., 1899), later models converged on iron oxides such as hematite (Cloud, 1973; James, 1954; reviewed in Rasmussen et al., 2017). Observations of chert bands and nodules, often targeted because they were early forming and relatively impermeable to later altering fluids (e.g., Clout & Simonson, 2005), resulted in the discoveries of microcrystalline (<1 μm) hematite particles that supported the conclusion that hematite was paragenetically the primary iron mineral (Ayres, 1972; Beukes & Gutzmer, 2008; Klein & Beukes, 1989; Spencer & Percival, 1952; Sun et al., 2015). This hematite was proposed to derive from the dehydration of ferric oxyhydroxide precipitates settling from suspension into silica gel on the ocean floor, with earlier hematite particles then getting replaced by coarser crystals of magnetite and siderite during diagenesis (Beukes & Gutzmer, 2008). This conclusion also made sense from a solubility point of view: oxidizing iron from soluble iron (ferrous $Fe^{2+}_{(aq)}$) to insoluble iron oxides (e.g., $Fe(III)(OH)_{3\ (s)}$) would act as a mechanism to transport iron into the sediments to form precursor BIFs. Previous research has extensively explored the processes that could produce these putative ferric oxyhydroxides in Archean oceans (e.g., see review by Posth et al., 2014), while other studies have used the adsorption behavior of trace metals and nutrients onto iron oxides to produce geologic records of seawater chemistry (e.g., Bjerrum & Canfield, 2002; Frei et al., 2009; Konhauser et al., 2009).

However, recent reexaminations of Neoarchean BIF-hosted chert from the ~2.5 Ga Hamersley Group in Western Australia and ~2.5 Ga Transvaal Supergroup in South Africa using nanoscale imaging and elemental analyses have led to the suggestion that iron silicate phases were actually present earlier than hematite (Rasmussen et al., 2015, 2016, 2017). Drill core samples of well-preserved BIFs and iron-rich cherts contained nanometer-sized iron silicate particles, as well as often bearing several morphologies of hematite and other iron minerals. Hematite either mineralized as a replacement texture such as iron oxide rims on iron silicate and iron-bearing carbonate crystals or occurred as individual 100 nm–10 μm equant or platy particles and defined primary bedding but transitioned vertically and horizontally to submicron iron silicate particles (Rasmussen et al., 2016). These iron silicates were identified as stilpnomelane and/or greenalite and occurred as randomly oriented plates that vary in size from <10 nm to 1 μm (Rasmussen et al., 2015, 2016, 2017). These observations were all highly suggestive of hematite being a secondary mineral, formed after primary iron silicates (Rasmussen et al., 2016), which was further explored and supported by recent experimental studies (Tosca et al., 2016).

If iron silicates are indeed the earliest mineral that we can identify in BIFs, then we need to better characterize them to understand what they record about the ancient marine system. Our goals were twofold: (1) to determine the exact mineralogy of the best preserved examples of these iron silicate inclusions, which serves to constrain Archean seawater chemistry; and (2) to assess the redox state of iron in these iron silicates, which can be indicative of the paleo-ocean oxidation state and potentially reveal any microbial involvement in the precipitation of these phases. We used a variety of bulk, microscale, and nanoscale techniques to characterize the iron silicate mineralogy and the iron redox state present in particles from the well-preserved examples of ancient BIF-hosted cherts. We find that the best preserved iron silicate nanoinclusions are greenalite with low and variable levels of Fe^{3+}, and these new results enable us to discuss several possible hypotheses to explain the deposition of primary low-Fe(III) greenalite that led to the formation of the most recognizable early Earth sediment, Banded Iron Formations.

2. Materials and Methods

Nanoparticle-bearing samples were acquired from ~2.5 Ga BIF and ferruginous chert hosted in well-preserved cores from Western Australia and South Africa (see Rasmussen et al., 2015, 2017; Sumner & Bowring, 1996, for core locations). These cores included ABDP9, GKF, DDH44, and Silvergrass, which have all undergone only low-grade metamorphism and are considered subgreenschist facies (Miyano & Beukes, 1984; Smith et al., 1982). Ferruginous cherts from ABDP9 and GKF were prioritized because they possessed the most finely laminated sections with the best level of detail of the many examined samples and were less recrystallized than BIF-hosted chert. Two samples were also chosen to ensure that our findings represented BIF mineralogy as well as ferruginous chert: DDH44 388.3 m was chosen as one of the best preserved Hamersley BIFs and Silvergrass 313.6 m was included as another example of a BIF with some well-preserved chert bands, although other bands showed recrystallization and late crystals of riebeckite and magnetite.

Samples were prepared as bulk powders, thin sections, and ~100 nm thick foils to examine the nanoparticles using a variety of chemical and structural characterization techniques. See supporting information for preparation and analytical details. Focused ion beam (FIB)-prepared foils for nanoscale analyses were produced from samples ABDP9 219.3 m and 288.2 m, GKF 327.2 m, and from the Silvergrass core at 313.6 m. The iron redox state of the FIB foils was examined at the nanoscale using synchrotron transmission X-ray microscopy at the iron L edge on the Spectromicroscopy beamline 101D-1 at the Canadian Light Source in Saskatoon, Canada (Cosmidis & Benzerara, 2014). Using this technique, we assessed the iron redox state across a single particle and compared the redox state variation between neighboring particles within any foil, following the Fe-silicate method and calibration established by Bourdelle et al. (2013). These nanoscale redox data were paired with subsequent transmission electron microscopy (TEM)-based examinations to confirm the particle scale mineralogy and assess the recrystallization extent of individual particles. Bright field TEM and high-angle annular dark-field scanning TEM images were collected to examine particle textures, and qualitative and quantitative energy dispersive spectroscopy maps, spectra, and point analyses were collected to help identify the nanoparticle mineralogy. Because the particles can be damaged by the electron beam, especially during electron diffraction, we analyzed high-resolution TEM images using a fast Fourier transform algorithm to produce diffractograms in which lattice spacing could be quantitatively measured and compared to iron silicate standards.

3. Results

We primarily used transmission-based microscopic and spectroscopic techniques to assess the morphology and crystal structure of the iron-rich inclusions, complemented by microscale and bulk spectroscopic and diffraction techniques. The iron silicate inclusions from five well-preserved samples derived from Australia and South Africa displayed differential recrystallization, with some samples (e.g., ABDP9 288.3 m) containing fairly pristine particles and other samples (e.g., ABDP9 219.3 m and GKF 327.2 m) having some highly recrystallized inclusions associated with chert cavities. Diffractograms yielded d-spacings corresponding to a 7 Å clay in most sections (Figure 1). This result was consistent with analyses that showed small 7 Å clay peaks in bulk powders containing nanoparticle inclusions (Figure S1). Fe X-ray absorption spectra plotted using Sixpack (Webb, 2005) were also consistent with iron in a silicate mineral (supporting information Figures S2 and S3). Using TEM-energy dispersive spectroscopy, we confirmed that these particles only contained Fe, Si, and O, with low and varying amounts of Mg and Al (Figures S4a–S4d and Table S1), indicating these were Fe-silicates such as the 7 Å layered Fe-silicates greenalite $[Fe_3^{2+}Si_2O_5(OH)_4]$ or cronstedtite $[(Fe^{2+},Fe^{3+})_3(Si,Fe^{3+})_2O_5(OH)_4]$. The 7 Å silicates also contained the ~20 Å structural modulation characteristic of greenalite (Figure 1) (Guggenheim et al., 1982). The integrated results from all of our multiscale independent analyses indicate that the structure and chemistry of the nanoparticles were consistent with greenalite.

Several other iron minerals were additionally observed. ABDP9 288 m2 contained siderite euhedra and ABDP9 219 m had two small pyrite crystals, but both appeared secondary to the greenalite as they were blocky crystals that cross cut greenalite nanoparticles. In contrast to the other sections, some silicate particles from section Silvergrass 313.6 m had 10 Å spacing (Figure 1). These diffraction results coincided with a different elemental pattern (Figure S4e). The data from this distinct set of particles were consistent with the presence of a 10 Å layered silicate containing K, Fe, Mg, and Al cations, like the complex hydrated phyllosilicate stilpnomelane $[(K,Ca,Na)(Fe,Mg,Al)_8(Si,Al)_{12}(O,OH)_{36}\cdot nH_2O]$ (Figures 1 and S4E). While commonly found in low-pressure, subgreenschist facies BIF, stilpnomelane is often considered a metamorphic mineral associated with greenschist facies or glaucophane-schist facies (Krivovichev, 2013). In BIFs, stilpnomelane is generally observed texturally as forming secondarily, associated with recrystallization and metamorphism (Feininger, 1984; Klein, 1974), and this Silvergrass sample in thin section appeared petrographically to be more recrystallized and altered. Therefore, we suggest that the stilpnomelane particles in Silvergrass 313.6 m are alteration products from earlier greenalite inclusions. Another possibility is that the stilpnomelane reflects detrital grains from volcanic sources (Haugaard et al., 2016; Laberge, 1986; Pickard, 2002). Because all 10 samples that we examined contained well-preserved greenalite encased in chert, our results indicate that greenalite was a primary mineral forming from Neoarchean seawater.

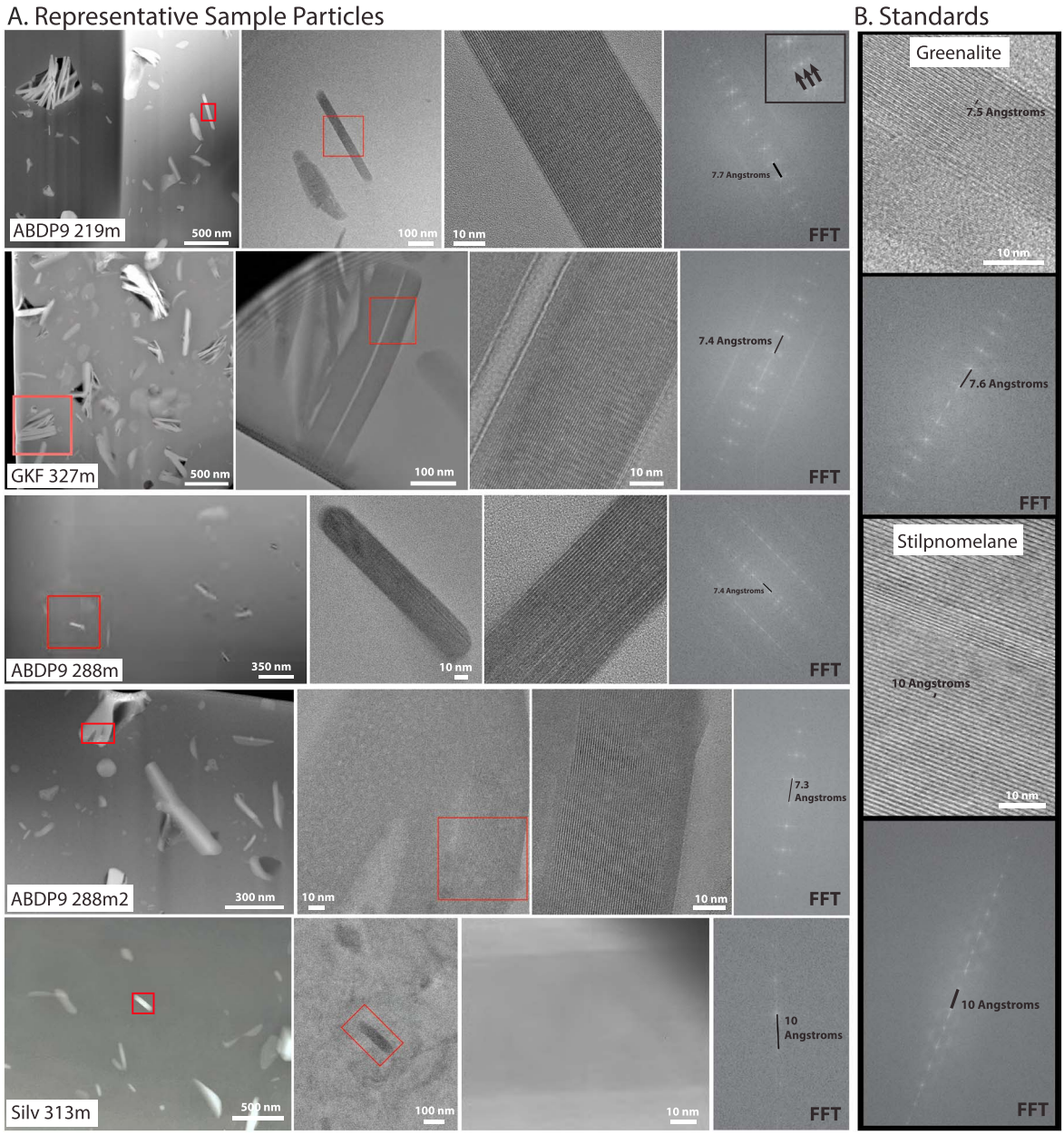

Figure 1. Transmission electron microscopy images and diffractograms of nanoparticle inclusions. (a) Five focused ion beam foils of representative particles. Images on left indicate particle analyzed using high-resolution transmission electron microscopy imaging (right images) and fast Fourier transform (FFT, right panel) to quantify the particle layering distance. Four samples had nanoparticles with d-spacings ~7.3–7.7 Å, while Silvergrass 313 m had some particles with 10 Å spaced layers. Inset with arrows for ABDP9 219 m indicate the ~20 Å superlattice reflections characteristic of greenalite. (b) Standards for greenalite and stilpnomelane show 7.6 Å spaced layers for Greenalite and 10 Å spaced layers for stilpnomelane.

The iron redox state of the iron silicate inclusions in these FIB foil samples were determined using scanning transmission X-ray spectromicroscopy at the Fe $L_{2,3}$ edge. We harnessed a novel iron redox mapping method to examine the variability of the iron redox state at a nanoscale. Following the protocol outlined in Bourdelle et al. (2013), Fe(III)/Fe_{Total} maps were produced across the iron-bearing nanoparticles (Figure 2) using the aXis2000 software (Hitchcock, 2014). This mapping indicated that the iron silicate inclusions were principally Fe(II), consistent with Fe K-edge analyses (Figure S5), but the nanoparticles also contained low levels of Fe(III). Across individual nanoparticles mapped for Fe(III) content, pixels ranged from 0% to >70% Fe(III)/Fe_{Total} (Figure 2). The most pristinely preserved particles, those fully encased in chert, had low ferric iron contents

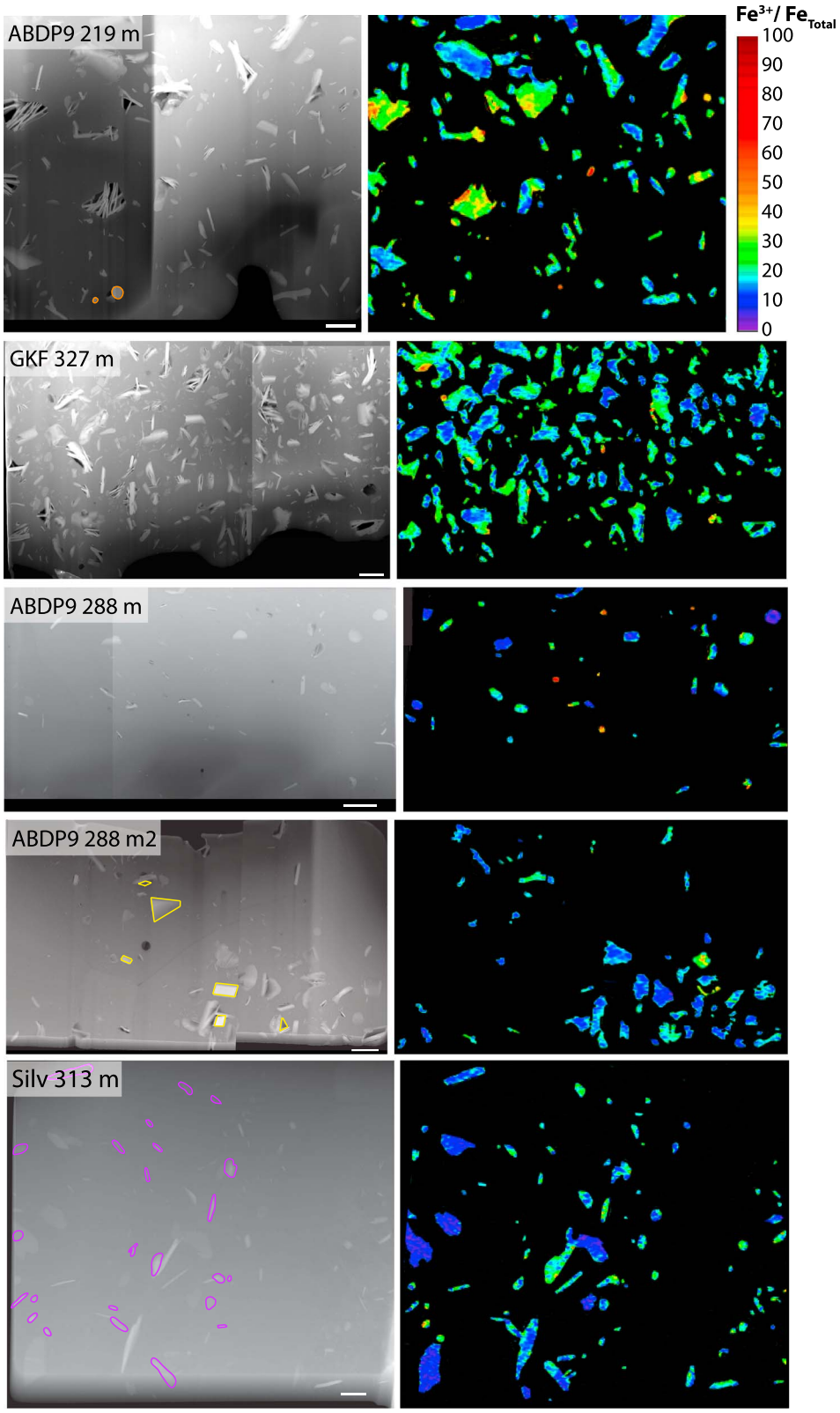

Figure 2. Iron redox maps of nanoparticle inclusions in chert sample focused ion beam foils imaged using scanning transmission electron microscopy (left column) and Fe(III)/Fe_{Total} redox maps (right column) constructed using multiple energy synchrotron transmission X-ray microscopy maps. Nongreenalite particles are outlined: pyrite crystals (orange) and siderite crystals (yellow) were excluded from redox analyses, but a different iron silicate (purple) was included in the iron silicate redox analysis. Scale bars 500 nm.

ranging from ~10% to 20% Fe(III)/Fe_{Total} (Figure 2). The low levels of Fe(III) varied both within individual particles and between particles and appeared unrelated to the pixel position in the particle, particle orientation, or particle location.

4. Discussion

One of our best windows into the chemistry and biology of early Earth's oceans is through understanding what chemical precipitates were forming directly from seawater. While iron oxyhydroxides were thought to be the dominant Fe minerals that initially precipitated and were therefore intensively studied for how they may reflect biological activities and elemental cycles (Bekker et al., 2014; Kappler & Newman, 2004; Konhauser et al., 2007; Posth et al., 2014), recent observations of nanoscale iron silicate inclusions in early diagenetic, low-porosity chert have called the existing model into question (Rasmussen et al., 2015, 2017). These iron silicates are interpreted to be paragenetically earlier than iron oxides (Rasmussen et al., 2016), stimulating new questions about what BIFs actually indicate about seawater chemistry and mineralization pathways.

Additional factors make these pervasive iron silicate inclusions a compelling initial mineral during BIF deposition. Iron silicates such as minnesotaite, greenalite, and stilpnomelane have long been identified in BIFs, but the consensus view categorized these as secondary minerals or derived from volcanic input (Beukes & Gutzmer, 2008; Fischer & Knoll, 2009; Haugaard et al., 2016; Klein, 2005). There had been speculation that primary iron silicates could form in deeper-water and more alkaline environments as ferrous iron and silica reacted, but these minerals were not thought to be the major primary iron phase in BIFs (e.g., Beukes & Gutzmer, 2008; Klein, 1974). However, primary magnetic remanences that should have been recorded in original hematite precipitates, if they stayed below 600°C, have never been found in the Australian Hamersley Group and South African Transvaal Supergroup BIFs (Abrajevitch et al., 2014; de Kock et al., 2009; Humbert et al., 2017; Li et al., 1993)—highly suggestive of hematite being emplaced secondarily. Additionally, with the probable elevated silica levels of the Archean ocean (Maliva et al., 2005; Siever, 1992; Stefurak et al., 2014), the mineralization of iron silicates is thermodynamically predicted (Bethke, 2002) from highly reducing oceans with $<10^{-56}$ atm of O_2 (Figure S7).

To better constrain these potentially primary Neoarchean minerals, we fully characterized the mineralogy and iron redox state of the best preserved iron silicate inclusions that have been discovered thus far. Ten samples from ~2.5 Ga BIFs and ferruginous cherts from diverse localities in Australia and South Africa contain a single identical iron silicate mineral: greenalite. From these observations, we argue that greenalite is the earliest iron mineral preserved in these cherts. Earlier hypotheses had suggested that iron was deposited in the sediments as a result of iron oxidation. In order to determine whether an oxidation state change was still relevant to understanding deposition of primary iron silicates, we examined whether Fe(III) was present in the greenalite particles and quantified how much ferric iron was present at the scale of individual particles. In the most unaltered particles, we found that greenalite was dominantly Fe(II) with 10–20% Fe(III). Fe(III) content was variable within individual particles and between particles. The possibility that these low levels of Fe(III) were secondarily acquired cannot be ruled out; however, the absence of a spatially coherent redox distribution suggests that this Fe(III) was an original component of the greenalite rather than oxidized by a secondary fluid front.

Our characterization of the Fe-rich nanoparticle inclusions enables us to consider and build on existing hypotheses to explore the genesis of low-Fe(III) greenalite preserved in early chert. In the following scenarios, our working hypothesis is that seawater silica (H_4SiO_4) was at saturation with amorphous silica ($10^{-2.71}$ M, Rimstidt & Barnes, 1980). Previous work has established that silica levels were significantly higher in the Archean oceans (Maliva et al., 2005; Siever, 1992) and observations of primary authigenic silica granules in Archean cherts (Stefurak et al., 2014, 2015) provide strong evidence for silica levels at saturation with amorphous silica. We thus assume amorphous silica was being deposited on the sea floor, encasing greenalite inclusions during the diagenetic transformation into chert nodules and bands. In the models described below, we primarily focus on various iron cycle hypotheses to result in the preservation of low-Fe(III) greenalite in chert.

1. A straightforward explanation for the deposition of greenalite nanoparticles is that the ferrous iron and silica concentrations of the ocean exceeded greenalite saturation (Figure 3(1)). The saturation of greenalite is set by its solubility constant, which can be calculated to lie at $10^{14.01}$ using estimates from Eugster &

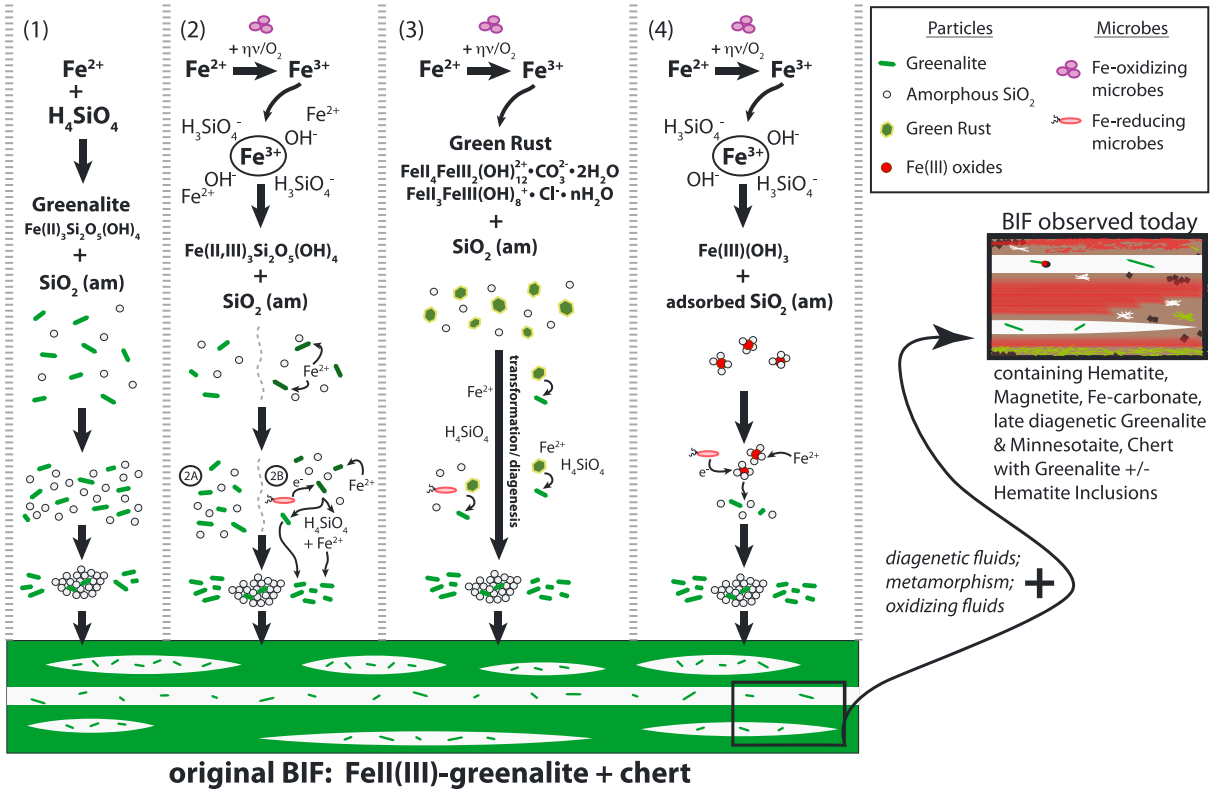

Figure 3. Mechanisms to produce low-Fe(III) greenalite in chert assuming seawater was at amorphous silica saturation, hypothetical pathways to form low-Fe(III) greenalite encased in chert are the following: (1) greenalite exceeded saturation chemistry and precipitated. (2) Precipitation of Fe(II,III) greenalite catalyzed by the oxidation of aqueous Fe^{2+}, either abiotically or biologically mediated. (A) Precipitation directly formed low-Fe(III) greenalite or (B) precipitation began as a high-Fe(III) greenalite, which then stabilized as low-Fe(III) greenalite. (3) Oxidation of Fe^{2+} formed metastable green rust, which then transformed into low-Fe(III) greenalite. (4) Oxidation of Fe^{2+} formed precursor iron oxides and silica, which then transformed into low-Fe(III) greenalite. BIF = banded iron formations.

Chou (1973). If we assume that dissolved silica was fixed at $10^{-2.71}$ M and pH at this time was ~7 (Halevy & Bachan, 2017), then greenalite would saturate when ferrous iron reached 30 nM (Figure S7). This estimate is likely far lower than the concentrations that metastable precursor phases would require to precipitate; however, it is useful to consider the thermodynamic predictions for greenalite precipitation. Alternatively, ferrous iron could remain below 30 nM and increases in pH could trigger the precipitation of greenalite. These iron concentrations are strikingly low and emphasize the ease with which greenalite should precipitate from the Neoarchean ocean—and suggest that greenalite precipitation would act as a limit to ferrous iron levels and pH.

The idea that greenalite was thermodynamically stable in the Neoarchean ocean expands on early suggestions for iron silicate precipitation in deep waters (Beukes & Gutzmer, 2008), which was also reproposed when iron silicates were discovered as abundant inclusions in chert (Rasmussen et al., 2015). A similar abiotic model has recently been explored experimentally by Tosca et al. (2016), who synthesized a protogreenalite gel under plausible Archean seawater conditions with high silica and iron concentrations at pHs $\geq$ 7.5. These experiments demonstrated that it is remarkably simple and favorable to precipitate a precursor silicate gel in anoxic, ferruginous, and silica-rich oceans (Tosca et al., 2016), and they suggested that alkaline hydrothermal waters upwelling into more acidic CO_2-buffered surface water would rapidly nucleate greenalite. Rasmussen et al. (2017) expanded on this pH-focused model but proposed flipping the environmental conditions: iron and silica delivered by more acidic vent fluids could then mix with more alkaline seawater, initiating the precipitation of greenalite.

2. Greenalite solubility is still not well constrained, and little is currently known about whether the presence of Fe(III) would enhance the precipitation of greenalite. However, it is hypothesized that in the iron-phosphate system, the oxidation of Fe(II) causes the precipitation of Fe(II,III)-phosphate minerals

(Cosmidis et al., 2014; Miot et al., 2009; Voegelin et al., 2013). Furthermore, earlier work has shown that iron silicates, including Fe(III) serpentine-member clays, can precipitate in silica-rich systems both abiotically and stimulated by bacterial surfaces (Konhauser & Ferris, 1996; Konhauser & Urrutia, 1999; Urrutia & Beveridge, 1994). If Fe(III) does change the thermodynamic properties of greenalite and makes precipitation more favorable, then it is possible that waters undersaturated with respect to Fe(II)-greenalite could have precipitated Fe(III)-bearing greenalite upon aqueous Fe^{2+} oxidation (Figure 3(2)). A variety of iron oxidation mechanisms are known, including abiotic UV radiation catalysis, microbial iron-oxidizing photosynthesis, and biologically mediated or abiotic interactions between ferrous iron and oxygen (e.g., see Konhauser et al., 2007). Oxidation of iron in ferruginous and silica-rich water could catalyze the precipitation of a low-Fe(III) greenalite phase that could then be preserved in amorphous silica gel, eventually mineralizing as greenalite inclusions in chert (Figure 3(2A)).

Alternatively, iron oxidation in silica-rich water could initially produce high-Fe(III) greenalite. However, in a ferruginous ocean, contact between Fe(III)-bearing clays and fluids with ferrous iron could reduce structural Fe(III) and increase the Fe(II) content of the mineral (Schaefer et al., 2011). Although we see no evidence for surface-associated Fe(III) phases, these should be produced if adsorbed Fe(II) was oxidized; however, if formed, such phases would be highly reactive in a reducing environment. A net chemical reduction of Fe(III)-bearing greenalite could occur both during descent of the particles through a ferruginous water column or in pore waters if reductants are present (Figure 3(2B)). The potential reactions described above could have led to a similar primary mineral assemblage as models 1 and 2A—initial BIFs dominated by low-Fe(III) greenalite and chert (Figure 3(2)). Additionally, Fe(III) in the silicate structure or Fe(III) phases associated with greenalite could have been reduced by bacterial respiration during early diagenesis, resulting in an isostructural transformation to lower-Fe(III) clays or reductive dissolution of the Fe-silicates into its constituent cations (Figure 3(2B)) (Dong et al., 2009).

3. A third model would also form low-Fe(III) greenalite as a stable mineral product, but from an initial Fe(II,III) precursor metastable phase: green rust $[Fe(II)_4Fe(III)_2(OH)_{12}^{2+}\bullet CO_3^{2-}\bullet 2H_2O$ or $Fe(II)_3Fe(III)(OH)_8^{+}\bullet Cl^{-}\bullet nH_2O]$ (Figure 3(3)), as suggested in a recent paper (Halevy et al., 2017). If a small proportion of aqueous iron is oxidized—by any biological or abiotic mechanism discussed above—in a highly ferruginous aqueous environment, then green rust is the metastable initial product that forms in both laboratory experiments and environmental settings (Halevy et al., 2017; Zegeye et al., 2012). Because green rust is a metastable phase, it would transform to secondary, stable phases (Halevy et al., 2017). Ferrous iron present in both the ocean and pore waters, as well as adsorbed and dissolved silica, could have subsequently induced the transformation of green rust into thermodynamically more favorable low-Fe(III) greenalite during particle descent and early diagenesis in the sediments (Figure 3(3)). Early diagenesis could also include iron-reducing microbes utilizing the oxidized iron in green rust and promoting the transformation of green rust into the more stable Fe(II)-rich greenalite. If the pore water conditions were supersaturated with respect to greenalite and the oxidation potential (Eh) of the system was low enough, then the predicted stable iron mineral to be preserved in the BIF sediments would be greenalite (Figure S7A).

4. Alternatively, it is possible that the oxidation of aqueous Fe(II) initially formed metastable Fe(III) oxides with adsorbed silica, similar to prior suggestions (Fischer & Knoll, 2009), which then stabilized as greenalite in the water column or sediments (Figure 3(4)). Indeed, experiments with modern iron-oxidizing phototrophs grown with 2 mM silica resulted in the formation of Fe(III)-oxyhydroxides, with some changes to morphology and crystallinity, silica substitution into the iron oxides, and coprecipitation of amorphous silica (Eickhoff et al., 2014; Gauger et al., 2016; Wu et al., 2014). It is notable that the formation of Fe(III) clays was not observed in these experiments, even with high silica levels. However, it is still an open question as to whether iron oxides and adsorbed silica would undergo dissolution and reprecipitation into low-Fe(III) greenalite under reducing conditions and/or through the activities of Fe-reducing microbes (Fischer & Knoll, 2009), as this has not conclusively been shown to occur (Posth et al., 2013, but see Aller et al., 1986).

It is currently difficult to resolve which model is most plausible to generate the low-Fe(III) greenalite that we observe. The first abiotic saturation hypothesis is appealing in its simplicity, and the low and variable levels of Fe(III) that we measured in the greenalite could be present as a result of the equilibrium environmental conditions at the time of formation or, alternatively, structural Fe(II) oxidation (Gorski et al., 2012) from secondary fluids post-lithification. Alternatively, the low Fe(III) that we measure in the greenalite could

Acknowledgments
Supplemental data and results can be found in the supporting information, and data used to generate figures can be found on the Deep Blue online repository (doi: 10.7302/Z2XS5SMK). We appreciate the contributions of Eric Ellison on Fe XANES acquisition and analysis and Tyler Kane for performing bulk XRD measurements and assisting with XRD analyses using JADE software. We additionally are grateful to S. Guggenheim for providing a greenalite standard and to George Rossman for contributing a standard for cronstedtite and for his mineralogical consultations, as well as the helpful feedback from Nicholas Tosca and an anonymous reviewer. Samuel Webb and Ryan Davis greatly helped with our data acquisition from SSRL and Jian Wang provided calibration and assistance for our STXM measurements at CLS. We additionally thank Franck Bourdelle who kindly helped us produce the Fe^{3+}/Fe_{TOTAL} maps. We acknowledge the Department of Mines and Petroleum, Western Australia, for access to drill hole ABDP9 and the Council for Geoscience (South Africa) for access to drill hole GKF. FIB and TEM analyses were performed at the Centre for Microscopy, Characterisation and Analysis, the University of Western Australia, a node of the Australian Microscopy and Microanalysis Research Facility funded from university and government sources. This research was funded by the Agouron Institute (Postdoctoral Fellowship) to J.E.J and the Rock-Powered Life NASA Astrobiology Institute (Cooperative Agreement NNA15BB02A). Portions of the research described in this paper was performed at the Canadian Light Source, which is supported by the Canada Foundation for Innovation, Natural Sciences and Engineering Research Council of Canada, the University of Saskatchewan, the Government of Saskatchewan, Western Economic Diversification Canada, the National Research Council Canada, and the Canadian Institutes of Health Research. Portions of this research were carried out at the Stanford Synchrotron Radiation Lightsource, SLAC National Accelerator Laboratory, which is supported by the U.S. Department of Energy, Office of Science, Office of Basic Energy Sciences under contract DE-AC02-76SF00515. The SSRL Structural Molecular Biology Program is supported by the DOE Office of Biological and Environmental Research and by the National Institute of Health, National Institute of General Medical Sciences (including P41GM103393).

signify original iron oxidation from UV radiation, iron-oxidizing photosynthesis, or interactions with low levels of oxygen. Another line of evidence for original Fe(III) present in greenalite or precursor phases may arise from the Fe-rich carbonates present in BIFs, which many have argued are products of early diagenesis, primarily based on the ^{12}C-enriched carbon isotopes and textures of these phases (Ayres, 1972; Becker & Clayton, 1972; Beukes et al., 1990; Dimroth & Chauvel, 1973; Fischer & Knoll, 2009; Johnson et al., 2013; Klein, 1974; Walker, 1984). Intriguingly, siderite is also found as a product from the reduction of Fe(III)-bearing clays (Dong et al., 2009; Komlos et al., 2007; Kostka et al., 1999). Therefore, hypotheses that involve a flux of oxidized iron—in Fe-silicates or other phases—reaching the sediments and potentially undergoing microbial reduction would be consistent with the arguments for early diagenetic Fe-rich carbonates in BIFs.

Distinguishing between hypotheses involving abiotic precipitation or iron oxidation followed by the stable mineralization of low-Fe(III) greenalite requires either further constraints on the solution chemistry and redox conditions of the 2.5 Ga ocean or more experimental data to measure what minerals actually precipitate in potential scenarios. Yet our detailed characterization of low-Fe(III) greenalite as the earliest iron phases in BIF sediments emplaces a firm target against which to compare experimental and environmental observations. For the primary mineral in equilibrium with the Neoarchean seawater to stabilize as greenalite rather than hematite, the deep ocean and/or pore water can be inferred to have an oxygen fugacity $<10^{-56}$ atm (Figure S7C)—inconsistent with the presence of extensive oxygenic photosynthesis. Going forward, to successfully recreate the chemistry and biology in the 2.5 Ga ocean, low-Fe(III) greenalite should be present in the stable mineral assemblage. Conversely, the presence of low-Fe(III) greenalite as a primary stable mineral 2.5 billion years ago should act as a constraint for future estimates of pH, ferrous iron, and silica concentrations in the Neoarchean ocean.

References

Abrajevitch, A., Pillans, B. J., & Roberts, A. P. (2014). Haematite pigmentation events and palaeomagnetic recording: Implications from the Pilbara Print Stone, Western Australia. *Geophysical Journal International*, *199*, 658–672.

Aller, R. C., Mackin, J. E., & Cox, R. T. Jr. (1986). Diagenesis of Fe and S in Amazon inner shelf muds: Apparent dominance of Fe reduction and implications for the genesis of ironstones. *Continental Shelf Research*, *6*(1–2), 263–289.

Ayres, D. E. (1972). Genesis of iron-bearing minerals in banded iron formation Mesobands in the Dales Gorge Member, Hamersley Group, Western Australia. *Economic Geology*, *67*(8), 1214–1233. https://doi.org/10.2113/gsecongeo.67.8.1214

Becker, R. H., & Clayton, R. N. (1972). Carbon isotopic evidence for the origin of a banded iron-formation in Western Australia. *Geochimica et Cosmochimica Acta*, *36*(5), 577–595. https://doi.org/10.1016/0016-7037(72)90077-4

Bekker, A., Planavsky, N. J., Krapež, B., Rasmussen, B., Hofmann, A., et al. (2014). Iron formations: Their origins and implications for ancient seawater chemistry. *Treatise Geochem. Second Ed.*, *9*, 561–628.

Bethke, C. M. (2002). *The geochemist's workbench: A user's guide to Rxn, Act2, Tact, React, and Gtplot* (4.0 ed.). Urbana, IL: University of Illinois.

Beukes, N. J. (1984). Sedimentology of the Kuruman and Griquatown iron-formations, Transvaal Supergroup, Griqualand West, South Africa. *Precambrian Research*, *24*(1), 47–84.

Beukes, N. J., & Gutzmer, J. (2008). Origin and paleoenvironmental significance of major iron formations at the Archean-Paleoproterozoic boundary. In S. Hagemann, et al. (Eds.), *Banded iron formation-related high-grade ore* (Vol. 15, pp. 5–47). Littleton, CO: Society of Economic Geologists, SEG Reviews.

Beukes, N. J., Klein, C., Kaufman, A. J., & Hayes, J. M. (1990). Carbonate petrography, kerogen distribution, and carbon and oxygen isotope variations in an early Proterozoic transition from limestone to iron-formation deposition, Transvaal Supergroup, South Africa. *Economic Geology and the Bulletin of the Society of Economic Geologists*, *85*(4), 663–690. https://doi.org/10.2113/gsecongeo.85.4.663

Bjerrum, C. J., & Canfield, D. E. (2002). Ocean productivity before about 1.9 Gyr ago limited by phosphorus adsorption onto iron oxides. *Nature*, *417*(6885), 159–162.

Bourdelle, F., Benzerara, K., Beyssac, O., Cosmidis, J., Neuville, D. R., Brown, G. E., & Paineau, E. (2013). Quantification of the ferric/ferrous iron ratio in silicates by scanning transmission X-ray microscopy at the Fe $L_{2,3}$ edges. *Contributions to Mineralogy and Petrology*, *166*(2), 423–434. https://doi.org/10.1007/s00410-013-0883-4

Cloud, P. (1973). Paleoecological significance of the banded iron-formation. *Economic Geology*, *68*(7), 1135–1143.

Clout, J. M. F., & Simonson, B. M. (2005). Precambrian iron formations and iron formation-hosted iron ore deposits. *Economic Geology*, *100th Anniversary Volume*, 643–679.

Cosmidis, J., & Benzerara, K. (2014). Soft X-ray scanning transmission spectromicroscopy. In E. DiMasi & L. B. Gower (Eds.), *Biomineralization sourcebook: Characterization of biominerals and biomimetic materials* (pp. 115–133). Boca Raton, FL: CRC Press. https://doi.org/10.1201/b16621-11

Cosmidis, J., Benzerara, K., Morin, G., Busigny, V., Lebeau, O., et al. (2014). Biomineralization of iron-phosphates in the water column of Lake Pavin (Massif Central, France). *Geochimica et Cosmochimica Acta*, *126*, 78–96.

de Kock, M. O., Evans, D. A. D., Kirschvink, J. L., Beukes, N. J., Rose, E., & Hilburn, I. (2009). Paleomagnetism of a Neoarchean-Paleoproterozoic carbonate ramp and carbonate platform succession (Transvaal Supergroup) from surface outcrop and drill core, Griqualand west region, South Africa. *Precambrian Research*, *169*(1–4), 80–99.

Dimroth, E., & Chauvel, J.-J. (1973). Petrography of the Sokoman Iron Formation in part of the Central Labrador Trough, Quebec, Canada. *GSA Bulletin*, *84*(1), 111–134. https://doi.org/10.1130/0016-7606(1973)84%3C111:POTSIF%3E2.0.CO;2

Dong, H., Jaisi, D. P., Kim, J., & Zhang, G. (2009). Microbe-clay mineral interactions. *American Mineralogist*, *94*(11–12), 1505–1519.

Eickhoff, M., Obst, M., Schröder, C., Hitchcock, A. P., Tyliszczak, T., Martinez, R. E., et al. (2014). Nickel partitioning in biogenic and abiogenic ferrihydrite: The influence of silica and implications for ancient environments. *Geochimica et Cosmochimica Acta*, *140*(Supplement C), 65–79. https://doi.org/10.1016/j.gca.2014.05.021

Eugster, H. P., & Chou, I.-M. (1973). The depositional environments of Precambrian banded iron-formations. *Economic Geology*, *68*(7), 1144–1168.

Farquhar, J., Zerkle, A. L., & Bekker, A. (2011). Geological constraints on the origin of oxygenic photosynthesis. *Photosynthesis Research*, *107*(1), 11–36.

Feininger, T. (1984). Stilpnomelane in metasomatic rocks associated with steatite and in regional schists, Quebec Appalachians. *The Canadian Mineralogist*, *22*(3), 423–435.

Fischer, W. W., & Knoll, A. H. (2009). An iron shuttle for deepwater silica in Late Archean and Early Paleoproterozoic iron formation. *Geological Society of America Bulletin*, *121*(1–2), 222–235.

Frei, R., Gaucher, C., Poulton, S. W., & Canfield, D. E. (2009). Fluctuations in Precambrian atmospheric oxygenation recorded by chromium isotopes. *Nature*, *461*(7261), 250–253.

Gauger, T., Byrne, J. M., Konhauser, K. O., Obst, M., Crowe, S., & Kappler, A. (2016). Influence of organics and silica on Fe(II) oxidation rates and cell–mineral aggregate formation by the green-sulfur Fe(II)-oxidizing bacterium Chlorobium ferrooxidans KoFox—Implications for Fe(II) oxidation in ancient oceans. *Earth and Planetary Science Letters*, *443*(supplement C), 81–89. https://doi.org/10.1016/j.epsl.2016.03.022

Gorski, C. A., Aeschbacher, M., Soltermann, D., Voegelin, A., Baeyens, B., Marques Fernandes, M., et al. (2012). Redox properties of structural Fe in clay minerals. 1. Electrochemical quantification of electron-donating and -accepting capacities of smectites. *Environmental Science & Technology*, *46*(17), 9360–9368. https://doi.org/10.1021/es3020138

Guggenheim, S., Bailey, S. W., Eggleton, R. A., & Wilkes, P. (1982). Structural aspects of greenalite and related minerals. *The Canadian Mineralogist*, *20*, 1–18.

Halevy, I., Alesker, M., Schuster, E. M., Popovitz-Biro, R., & Feldman, Y. (2017). A key role for green rust in the Precambrian oceans and the genesis of iron formations. *Nature Geoscience*, *10*(2), 135–139.

Halevy, I., & Bachan, A. (2017). The geologic history of seawater pH. *Science*, *355*(6329), 1069–1071.

Haugaard, R., Pecoits, E., Lalonde, S., Rouxel, O., & Konhauser, K. (2016). The Joffre banded iron formation, Hamersley Group, Western Australia: Assessing the palaeoenvironment through detailed petrology and chemostratigraphy. *Precambrian Research*, *273*(supplement C), 12–37. https://doi.org/10.1016/j.precamres.2015.10.024

Hitchcock A. P. (2014). aXis2000 is written in Interactive Data Language (IDL). It is available free for non-commercial use from <http://unicorn.mcmaster.ca/aXis2000.html/>

Humbert, F., Sonnette, L., de Kock, M. O., Robion, P., Horng, C. S., et al. (2017). Palaeomagnetism of the early Palaeoproterozoic, volcanic Hekpoort Formation (Transvaal Supergroup) of the Kaapvaal craton, South Africa. *Geophysical Journal International*, *209*(2), 842–865.

James, H. L. (1954). Sedimentary facies of iron-formation. *Economic Geology and the Bulletin of the Society of Economic Geologists*, *49*(3), 235–293.

Johnson, C. M., Ludois, J. M., Beard, B. L., Beukes, N. J., & Heimann, A. (2013). Iron formation carbonates: Paleoceanographic proxy or recorder of microbial diagenesis? *Geology*, *41*(11), 1147–1150.

Johnson, J. E., Gerpheide, A., Lamb, M. P., & Fischer, W. W. (2014). O_2 constraints from Paleoproterozoic detrital pyrite and uraninite. *Geological Society of America Bulletin*, *126*(5–6), 813–830. https://doi.org/10.1130/B30949.1

Kappler, A., & Newman, D. K. (2004). Formation of Fe(III)-minerals by Fe(II)-oxidizing photoautotrophic bacteria. *Geochimica et Cosmochimica Acta*, *68*(6), 1217–1226. https://doi.org/10.1016/j.gca.2003.09.006

Klein, C. (1974). Greenalite, stilpnomelane, minnesotaite, crocidolite and carbonates in a very low-grade metamorphic Precambrian iron formation. *The Canadian Mineralogist*, *12*(7), 475–498.

Klein, C. (2005). Some Precambrian banded iron-formations (BIFs) from around the world: Their age, geologic setting, mineralogy, metamorphism, geochemistry, and origins. *American Mineralogist*, *90*(10), 1473–1499.

Klein, C., & Beukes, N. J. (1989). Geochemistry and sedimentology of a facies transition from limestone to iron-formation deposition in the early Proterozoic Transvaal Supergroup, South Africa. *Economic Geology*, *84*(7), 1733–1774.

Komlos, J., Kukkadapu, R. K., Zachara, J. M., & Jaffé, P. R. (2007). Biostimulation of iron reduction and subsequent oxidation of sediment containing Fe-silicates and Fe-oxides: Effect of redox cycling on Fe(III) bioreduction. *Water Research*, *41*(13), 2996–3004.

Konhauser, K. O., Amskold, L., Lalonde, S. V., Posth, N. R., Kappler, A., & Anbar, A. (2007). Decoupling photochemical Fe(II) oxidation from shallow-water BIF deposition. *Earth and Planetary Science Letters*, *258*(1-2), 87–100. https://doi.org/10.1016/j.epsl.2007.03.026

Konhauser, K. O., & Ferris, F. G. (1996). Diversity of iron and silica precipitation by microbial mats in hydrothermal waters, Iceland: Implications for Precambrian iron formations. *Geology*, *24*(4), 323–326. https://doi.org/10.1130/0091-7613(1996)024%3C0323:DOIASP%3E2.3.CO;2

Konhauser, K. O., Pecoits, E., Lalonde, S. V., Papineau, D., Nisbet, E. G., et al. (2009). Oceanic nickel depletion and a methanogen famine before the Great Oxidation Event. *Nature*, *458*(7239), 750–753.

Konhauser, K. O., & Urrutia, M. M. (1999). Bacterial clay authigenesis: A common biogeochemical process. *Chemical Geology*, *161*(4), 399–413.

Kostka, J. E., Haefele, E., Viehweger, R., & Stucki, J. W. (1999). Respiration and dissolution of iron(III)-containing clay minerals by bacteria. *Environmental Science & Technology*, *33*(18), 3127–3133.

Krivovichev, S. V. (2013). Structural complexity of minerals: Information storage and processing in the mineral world. *Mineralogical Magazine*, *77*(3), 275–326.

Laberge, G. L. (1986). A model for the biological precipitation of Precambrian iron-formation. http://adsabs.harvard.edu/abs/1986ecgw.work...71L

Leith, C. K. (1903). The Mesabi iron-bearing district of Minnesota. *U.S. Geological Survey Monograph*, *43*. (316 pp.).

Li, Z., Powell, C., & Bowman, R. (1993). Timing and genesis of Hamersley iron-ore deposits. *Exploration Geophysics*, *24*(4), 631–636. https://doi.org/10.1071/EG993631

Maliva, R. G., Knoll, A. H., & Simonson, B. M. (2005). Secular change in the Precambrian silica cycle: Insights from chert petrology. *GSA Bulletin*, *117*(7), 835–845. https://doi.org/10.1130/B25555.1

Miot, J., Benzerara, K., Morin, G., Kappler, A., Bernard, S., et al. (2009). Iron biomineralization by anaerobic neutrophilic iron-oxidizing bacteria. *Geochimica et Cosmochimica Acta*, *73*(3), 696–711.

Miyano, T., & Beukes, N. J. (1984). Phase relations of stilpnomelane, ferri-annite, and riebeckite in very low-grade metamorphosed iron-formations. *South African Journal of Geology*, *87*(2), 111–124.

Pickard, A. L. (2002). SHRIMP U–Pb zircon ages of tuffaceous mudrocks in the Brockman Iron Formation of the Hamersley Range, Western Australia. *Australian Journal of Earth Sciences*, *49*(3), 491–507.

Posth, N. R., Canfield, D. E., & Kappler, A. (2014). Biogenic Fe(III) minerals: From formation to diagenesis and preservation in the rock record. *Earth Science Reviews*, *135*(Supplement C), 103–121. https://doi.org/10.1016/j.earscirev.2014.03.012

Posth, N. R., Köhler, I., Swanner, D. E., Schröder, C., Wellmann, E., et al. (2013). Simulating Precambrian banded iron formation diagenesis. *Chemical Geology*, *362*(Supplement C), 66–73. https://doi.org/10.1016/j.chemgeo.2013.05.031

Prasad, N., & Roscoe, S. M. (1996). Evidence of anoxic to oxic atmospheric change during 2.45-2.22 Ga from lower and upper sub-Huronian paleosols, Canada. *Catena*, *27*(2), 105–121.

Pufahl, P. K., & Hiatt, E. E. (2012). Oxygenation of the Earth's atmosphere–ocean system: A review of physical and chemical sedimentologic responses. *Marine and Petroleum Geology*, *32*(1), 1–20.

Rasmussen, B., & Buick, R. (1999). Redox state of the Archean atmosphere: Evidence from detrital heavy minerals in ca. 3250–2750 Ma sandstones from the Pilbara Craton, Australia. *Geology*, *27*(2), 115–118. https://doi.org/10.1130/0091-7613(1999)027%3C0115:RSOTAA%3E2.3.CO;2

Rasmussen, B., Krapež, B., Muhling, J. R., & Suvorova, A. (2015). Precipitation of iron silicate nanoparticles in early Precambrian oceans marks Earth's first iron age. *Geology*, *43*, 303–306.

Rasmussen, B., Muhling, J. R., Suvorova, A., & Krapež, B. (2016). Dust to dust: Evidence for the formation of "primary" hematite dust in banded iron formations via oxidation of iron silicate nanoparticles. *Precambrian Research*, *284*(Supplement C), 49–63. https://doi.org/10.1016/j.precamres.2016.07.003

Rasmussen, B., Muhling, J. R., Suvorova, A., & Krapež, B. (2017). Greenalite precipitation linked to the deposition of banded iron formations downslope from a late Archean carbonate platform. *Precambrian Research*, *290*(Supplement C), 49–62. https://doi.org/10.1016/j.precamres.2016.12.005

Rimstidt, J. D., & Barnes, H. L. (1980). The kinetics of silica-water reactions. *Geochimica et Cosmochimica Acta*, *44*(11), 1683–1699.

Rye, R., & Holland, H. D. (1998). Paleosols and the evolution of atmospheric oxygen: A critical review. *American Journal of Science*, *298*(8), 621–672.

Schaefer, M. V., Gorski, C. A., & Scherer, M. M. (2011). Spectroscopic evidence for interfacial Fe(II)−Fe(III) electron transfer in a clay mineral. *Environmental Science & Technology*, *45*(2), 540–545.

Siever, R. (1992). The silica cycle in the Precambrian. *Geochimica et Cosmochimica Acta*, *56*(8), 3265–3272.

Simonson, B. M. (2003). Origin and evolution of large Precambrian iron formations. In M. A. Chan & A. W. Archer (Eds.), *Extreme depositional environments: Mega end members in geologic time*, *Geological Society of America Special Paper* (Vol. 370, pp. 231–244). Boulder, CO.

Smith, R. E., Perdrix, J. L., & Parks, T. C. (1982). Burial metamorphism in the Hamersley Basin, Western Australia. *Journal of Petrology*, *23*(1), 75–102.

Spencer, E., & Percival, F. G. (1952). The structure and origin of the banded hematite jaspers of Singhbhum, India. *Economic Geology*, *47*(4), 365–383.

Spurr, J. E. (1894). The iron-bearing rocks of the Mesabi Range in Minnesota. 10

Stefurak, E. J. T., Lowe, D. R., Zentner, D., & Fischer, W. W. (2014). Primary silica granules—A new mode of Paleoarchean sedimentation. *Geology*, *42*(4), 283–286.

Stefurak, E. J. T., Lowe, D. R., Zentner, D., & Fischer, W. W. (2015). Sedimentology and geochemistry of Archean silica granules. *GSA Bulletin*, *127*(7–8), 1090–1107.

Sumner, D. Y., & Bowring, S. A. (1996). U-Pb geochronologic constraints on deposition of the Campbellrand subgroup, Transvaal Supergroup, South Africa. *Precambrian Research*, *79*(1–2), 25–35.

Sun, S., Konhauser, K. O., Kappler, A., & Li, Y.-L. (2015). Primary hematite in Neoarchean to Paleoproterozoic oceans. *GSA Bulletin*, *127*(5–6), 850–861.

Tosca, N. J., Guggenheim, S., & Pufahl, P. K. (2016). An authigenic origin for Precambrian greenalite: Implications for iron formation and the chemistry of ancient seawater. *GSA Bulletin*, *128*(3–4), 511–530.

Urrutia, M. M., & Beveridge, T. J. (1994). Formation of fine-grained metal and silicate precipitates on a bacterial surface (Bacillus subtilis). *Chemical Geology*, *116*(3–4), 261–280.

Voegelin, A., Senn, A.-C., Kaegi, R., Hug, S. J., & Mangold, S. (2013). Dynamic Fe-precipitate formation induced by Fe(II) oxidation in aerated phosphate-containing water. *Geochimica et Cosmochimica Acta*, *117*(Supplement C), 216–231. https://doi.org/10.1016/j.gca.2013.04.022

Walker, J. C. G. (1984). Suboxic diagenesis in banded iron formations. *Nature*, *309*(5966), 340–342.

Webb, S. M. (2005). SIXpack: A graphical user interface for XAS analysis using IFEFFIT. *Physica Scripta*, *2005*(T115), 1011.

Winchell, N. H., Grant, U. S., Todd, J. E., Upham, W., & Winchell, H. V. (1899). The geology of Minnesota. *Volume 4 of the Final Report*. *4*

Wu, W., Swanner, E. D., Hao, L., Zeitvogel, F., Obst, M., et al. (2014). Characterization of the physiology and cell-mineral interactions of the marine anoxygenic phototrophic Fe(II) oxidizer Rhodovulum iodosum--implications for Precambrian Fe(II) oxidation. *FEMS Microbiology Ecology*, *88*(3), 503–515.

Zegeye, A., Bonneville, S., Benning, L. G., Sturm, A., Fowle, D. A., et al. (2012). Green rust formation controls nutrient availability in a ferruginous water column. *Geology*, *40*(7), 599–602.